A Framework for Array Shape Reconstruction Through Mutual Coupling

Austin Fikes, *Graduate Student Member, IEEE*, Oren S. Mizrahi, *Graduate Student Member, IEEE*, and Ali Hajimiri, *Fellow, IEEE*

Abstract—**Flexible phased arrays potentially enable diverse applications not permitted by rigid systems; however, they introduce ambiguity in antenna element positions. If this position ambiguity can be overcome, flexible arrays can perform the full suite of array functions: beam steering, wavefront engineering, and beam focusing. Furthermore, shape reconstructions of arrays can be used for applications beyond beamforming. We propose a framework to reconstruct the shape of a flexible array that only uses mutual coupling measurements and does not require additional sensors or functionalities in the system. We discuss the approach, a two-step algorithm, which is highly modular and can be implemented in a variety of phased array systems. To demonstrate the accuracy of the approach, we present results from two passive 2.5-GHz phased array setups using dipole and patch antennas, as well as a 10-GHz (active) integrated circuit flexible phased array, and demonstrate the accuracy of the approach in this system. In all cases, the algorithm reconstructs the antenna shape accurately, with average position errors of approximately 6% of the wavelength. This article can serve as the beginning of the broad study of shape reconstruction algorithms and their applications.**

Index Terms—**Conformal antennas, convex optimization, Euclidean distance matrix (EDM), flexible electronics, integrated circuits, phased array, semidefinite programming, shape calibration, shape reconstruction.**

I. INTRODUCTION

ANTENNA arrays continue to play a growing role in a broad range of applications, from communications [1], [2], sensing [3], [4], ranging [5], [6], power transfer [7], projections [8], and imaging [9]. In addition to planar arrays, conformal arrays, which are rigidly fixed to a nonplanar surface, have long been used in low profile (aerodynamically and/or visually) radio frequency (RF) systems [10], [11] [12], mostly for streamlining purposes. In mechanically static arrays, unusual shape and orientation of array elements are analyzed and accounted for during the design phase as these systems are used for a single, rigid shape. With an unusual

but known shape array, pattern synthesis is well-studied and has been accomplished using geometric analysis [13], [14] and various optimization algorithms [15], including genetic algorithms [16]–[18]. While these techniques are effective, array shapes may not be static and known. Emerging applications using *flexible* microwave and mm-wave antenna arrays in wearables and lightweight, deployable apertures in space [19] change shape dynamically [20], requiring capabilities beyond conventional static conformal arrays. Flexible phased arrays, which can constantly change shape during deployment and operation, also suffer from irregular element position and orientation. However, their antenna positions may not be known in advance and accounted for during design. As such, flexible phased arrays must be able to determine their shape and dynamically update phases to control beam coherence and direction during operation.

An example of a flexible phased array is shown in Fig. 1. Flexible arrays could operate while curling with biological and mechanical joints or while fluttering in the wind if fast and accurate array shape reconstruction can be achieved. In other systems, an array that can accurately reconstruct its own shape may be used as a sensor itself in applications involving gaming, haptic human–machine interfaces, biomedical sensing, and so on. Shape reconstruction is significantly more general than shape calibration, instances of which have been shown in the past [21]. Shape calibration refers to adjustments of element excitation phases to account for changes in relative element position and orientation within the array. Without shape calibration, the beam-forming, beam-steering, beam-focusing, arbitrary wavefront generation, and interference suppression capabilities of a flexible phased array quickly disappear. Shape calibration of flexible arrays using ancillary resistive strain sensors was shown in [22]. These additional sensors increase system complexity by incorporating a new sensing domain and utilizing hardware not already present in phased array systems. In addition, each resistive strain sensor only offers a single measurement value. For an array with complex bending geometry (having high sinuosity or lacking bilateral symmetry), a single, localized measurement will not accurately capture the array shape. Designing a flexible phased array with a limited number of ancillary sensors requires knowledge of the expected space of curvatures that the array surface will experience during design, limiting the applications of such an array.

Superseding prior calibration approaches, shape reconstruction describes a more complete and more difficult task: full
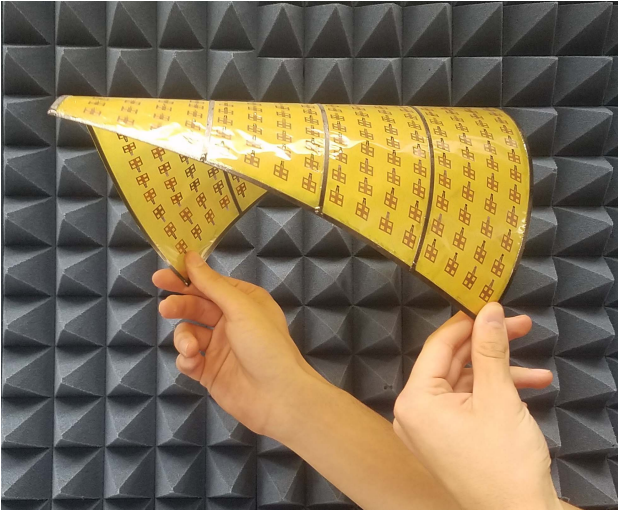
Fig. 1.   2-D flexible phased array antenna sheet with 256 10-GHz patch antennas.

determination of the shape of the array and the surface to which it is confirmed. In this work, we propose a framework for performing shape reconstruction only from local measurements of mutual coupling between elements in a flexible phased array. While phased arrays are typically designed to direct an electronically steerable beam of microwave power toward a far-field target, some fraction of the power radiated by one element in the array is absorbed by the other elements. This incidental power transmission is called mutual coupling. While, in extreme cases, it may be detrimental to array performance, mutual coupling provides information about the state of elements within the array. Shipley and Woods [23] and Bekers *et al.* [24] use mutual coupling measurements in an array with known shape and symmetry to determine the phase offset of elements within the array. Mutual coupling shape reconstruction transposes the problem: using mutual coupling measurements to determine the relative position of elements in the array.

In most practical cases, mutual coupling measurements contain sufficient information for array shape reconstruction, but an analytical and algorithmic framework is required to turn an interelement coupling matrix into element positions. We previously presented an approach in [25]; in this article, we propose a two-step, modular framework that is adaptable to different algorithmic approaches accounting for different sets of antenna properties and physical constraints. We propose an algorithm for each of these two steps. This article represents a more comprehensive discussion of the general framework, a more specific discussion of the algorithms, and presents results from three different arrays instead of only two.

The framework, using our proposed algorithms, is successfully demonstrated on two different passive arrays with different radiators. To demonstrate a realistic system-level implementation of such algorithms, we designed and built a flexible, active 10-GHz array using monolithic RF integrated circuits (RFICs). RFICs provide timing synchronization, frequency synthesis, signal amplification, digitization, and a multitude of digital control functions with a millimeter-scale footprint. With this density of complex

functions, discrete components can be removed, avoiding their bulk and rigidity, which would be prohibitive for a truly flexible design. The integrated circuit-based flexible phased array presented in Section VI represents a new paradigm in array design, only recently enabled by the proliferation of RFICs. Before discussing the RFIC array, we describe the framework and the motivations guiding our implementation.

II. FRAMEWORK OVERVIEW

A. Overview

Fig. 2 illustrates the modular framework for mutual coupling-based shape reconstruction. The framework begins with mutual coupling data represented as a matrix. The first step of the framework, called physical constraint mapping (PCM), processes the mutual coupling information to produce physical constraints of the array shape, such as element distances, mutual angles, or local curvatures. These physical constraints can be represented in different formats (matrix, etc.), but all contain the necessary information to reconstruct the shape. The second step, called array shape construction (ASC), utilizes the physical constraints to generate the actual positions of all elements and, thus, the array shape. This is, of course, the goal and purpose of this framework.

In this article, we present the framework and specific examples of PCM and ASC algorithms. We define the following terms: a mutual coupling matrix $S \in \mathbb{C}^{N \times N}$, a physical constraint matrix $B \in \mathbb{R}^{N \times N}$, and a position matrix $X \in \mathbb{R}^{d \times N}$, where N denotes the number of array elements and d denotes the number of physical dimensions that we expect our array to live in.[1] While the framework is general, in this article, we present results for flexible phased arrays with a single row of $N = 8$ elements that we will assume can only live in $d = 2$ dimensions. We will demonstrate that the flexibility of this framework allows for the reconstruction of planar phased arrays with arbitrary N that can potentially live in $d = 3$ dimensions.

The choice of algorithm for PCM and ASC is almost entirely dependent on the primary physical constraint that we choose to use (e.g., relative distances or curvatures). The freedom to choose B gives this framework much of its modularity; different physical constraints will be better suited for different antenna systems. In this work, we consider the use of Euclidean distance matrices (EDMs) as candidates for the physical constraint matrix [26].

An EDM, $E \in \mathbb{R}^{N \times N}$, is defined as

$$E_{mn} = |\vec{r}_m - \vec{r}_n|^2 \tag{1}$$

where $\vec{r}_n$ ($n \in \{1, 2, \ldots, N\}$) is the position vector associated with point n. The matrix describes the squared distance between points in a d-dimensional point cloud. EDMs are apt candidates for B because we can use known relationships between coupling and distance to devise the PCM algorithm and use existing algorithms for determining position from relative distance.

As we will discuss in the following, distance impacts both the phase and power of mutual coupling measurements.
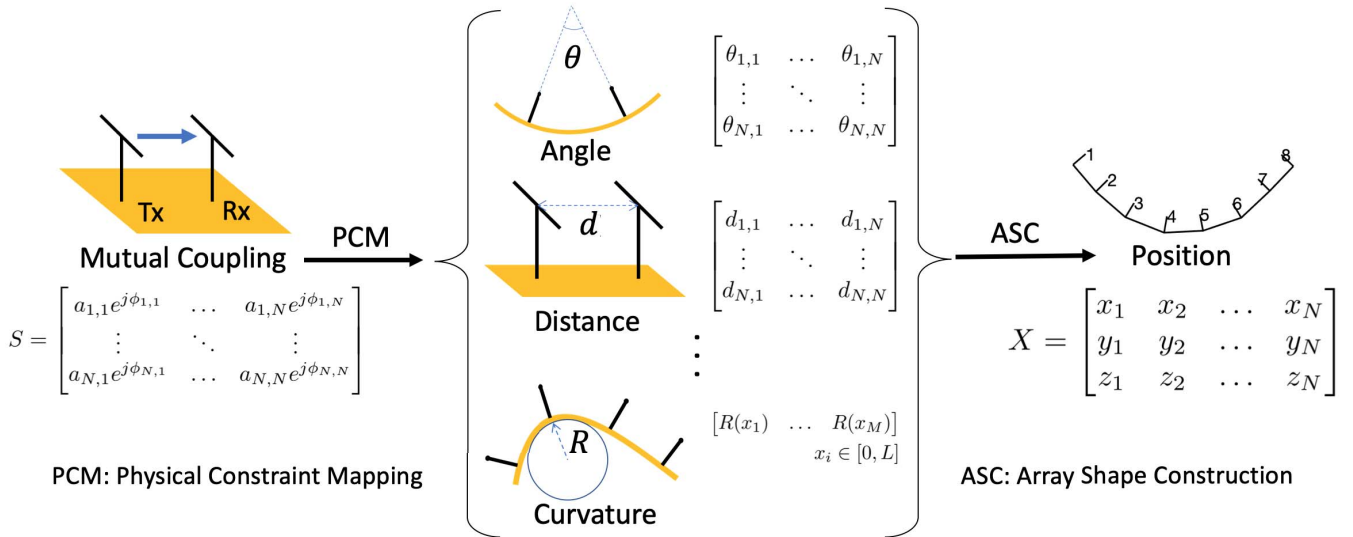
[1]$d \in \{1, 2, 3\}$.

Fig. 2. Block diagram of our framework for mutual coupling-based shape reconstruction.

We propose an algorithm, called Spiral Match, as a candidate for PCM. Moreover, the problem of solving for the relative positions of an arbitrary number of points in an arbitrary number of dimensions given an EDM, E, is critical to a number of applications and, thus, is well-studied [26]. We have a wealth of options for ASC that each accounts for different types of EDMs; for this system, we use a semidefinite optimization to solve for the relative position.

B. Mutual Coupling Model

Accurate mapping of coupling measurements to physical parameters of the array (PCM in Fig. 2) is critical for proper shape reconstruction. The PCM algorithm presented in this work is called Spiral Match (discussed in detail in Section III) and maps the measured complex-valued coupling to a distance between the phase centers of the elements. Near- and far-field electromagnetic interactions among the elements and with the environment can lead to a rich and sometimes nontrivial behavior for mutual coupling. Reactive fields, occlusion (blocked line of sight), surface waves, and multipath reflections of the ground plane, other elements, and nearby objects could affect the observed coupling between elements. The exact modeling of these effects is challenging in simple, ideal scenarios and is impractical if not impossible in the continuously changing context of a flexible phased array. Fortunately, these effects are second order in many intra-array coupling scenarios, where a far-field-like propagation mode dominates. Instead of an electromagnetically complete coupling model, we aim to create a simplified model with sufficient accuracy for shape reconstruction and adaptability for use with a variety of element radiator types.

The underlying philosophy behind Spiral Match is to match the measured coupling to distance using far-field properties of the element antennas as the individual antenna properties can be easily measured and are relatively insensitive to array shape. We start by approximating the coupling between antennas i and j in terms of the electric field of a far-field propagating

plane wave, i.e.,

$$S\left(|\vec{l_{mn}}|\right) \approx \frac{A}{|\vec{l_{mn}}|}e^{-j\left(\omega t + k|\vec{l_{mn}}|\right)} \qquad (2)$$

where $|\vec{l_{mn}}|$ is the linear distance between antennas m and n, k is the wavenumber, ω is the angular frequency, and A is an arbitrary amplitude scaling factor. It is assumed that phase grows linearly with distance between antennas ($|\vec{l_{mn}}|$), and the coupled power falls off as ($1/|\vec{l_{mn}}|^2$).

To evaluate this approximation, a simple study is performed with two 2.5-GHz ground plane backed folded dipole antennas (as described in detail in Section V-B). The coupling between dipole antennas was measured versus their distance, as shown in Fig. 3(a). Note that the ground plane is modified to maintain continuity at all distances. The coupling power and phase are plotted in Fig. 3(b) and (c). The measured coupling power is accompanied by two trendlines: the first follows the Friis ($1/|\vec{l_{mn}}|^2$) trend, the second follows a ($1/|\vec{l_{mn}}|^4$) trend.[2]

The coupling phase measurements roughly follow the linear trend predicted by the expression for a far-field propagating wave. Fig. 4 compares the pair measurement results to the coupling measurements between elements in a flat, eight-element 1-D array of the same folded dipoles with a pitch of 72 mm. Since the element pitch is fixed, in-array phase measurements only exist at multiples of 72 mm. These measurements also follow the linear model, suggesting that the presence of other elements in the array does not significantly disturb the phase of the propagation. While the measured phases in the study

---

[2]This ($1/|\vec{l_{mn}}|^4$) trend is commonly observed for communications systems with signals traveling long distances over an infinite conductive or lossy surface (usually the earth) [27]. For close distances, the measured coupling follows the ($1/|\vec{l_{mn}}|^4$) as the ground plane approximates an infinite conductive surface. However, as the distance between antennas increases, the infinite surface approximation no longer holds as the ground plane becomes relatively narrow, and the measured coupling returns to the ($1/|\vec{l_{mn}}|^2$) trend. This change in the distance exponent has a relatively small effect on the final shape reconstruction accuracy but emerges from a known, measurable phenomenon and can be incorporated into Spiral Match for a given array without much added modeling complexity.
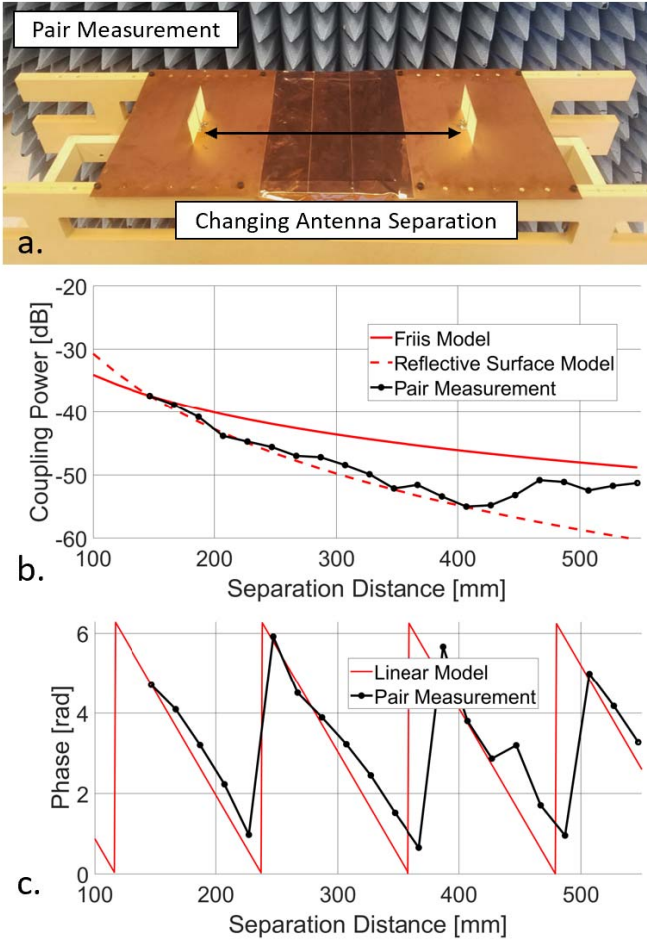
Fig. 3. (a) Antenna pair coupling study test setup. The continuous ground plane is maintained for all antenna distances. (b) Coupling power measurement compared with two different propagation models. Measurement averaged over the bandwidth from 2.3 to 2.7 GHz. (c) Coupling phase measurement plot. Antenna pair measurements compared with far-field linear phase propagation model. Measurement is at 2.48 GHz. In both the power and phase plots, linear model traces are normalized to the first measured distance.

Fig. 4. (a) Ground plane backed dipole array. (b) Unwrapped coupling phase measurement plot. In-array measured phased is compared to antenna pair measurements and far-field linear phase propagation model. Measurement is at 2.48 GHz. Traces are normalized to the first pair measurement distance.

do not match the linear model precisely, they do suggest that the trend holds.

While a more accurate and complex phase model *could* be developed, there is a fundamental tradeoff between the specificity of the antenna models and the generality of the algorithm; we have taken the position of keeping the model more general.

Under the coupling scenarios of Fig. 3, the elements experience relative position changes but no relative rotation. However, when a flexible phased array is bent, its elements experience changes in both position and orientation. To account for the change in coupling due to this rotation, we employ the far-field radiation pattern of the element antennas. Element radiation patterns can be determined through analysis, simulation, or measurement.

We will demonstrate that, although far-field phase propagation and radiation pattern are imperfect models of the coupling between elements within a phased array, they can be used to produce accurate shape reconstructions.
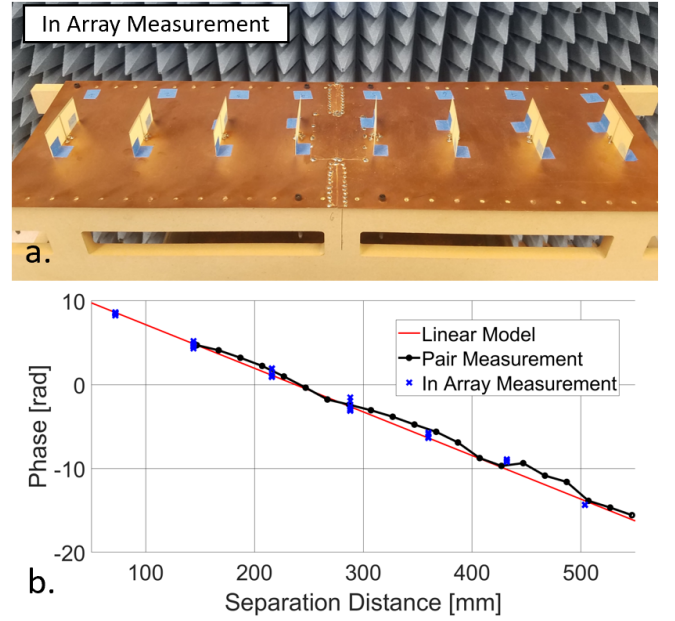
With the motivation for and justifications of the Spiral Match clarified, Section III details its implementation and the nuances that emerge.

III. SPIRAL MATCH

In this section, we will discuss the details of Spiral Match, which is a candidate for PCM. The name Spiral Match is inspired by the spiral shape generated in a polar plot of the decaying amplitude and rotating phase versus distance of propagating waves.

A. Definitions and Assumptions

Our overall goal is to generate a bijection (i.e., a one-to-one correspondence) between mutual coupling and distance. We begin by modeling the raw mutual coupling matrix $S \in \mathbb{C}^{N \times N}$ for a 1-D phased array[3] as

$$S_{mn} = \frac{a_m D_m(\theta_{mn}) a_j D_n(\theta_{nm})}{|\vec{l}_{mn}|} e^{-j\left(\phi_m + \phi_n + k|\vec{l}_{mn}|\right)} \quad (3)$$

$$\theta_{mn} = \cos^{-1}\left(\frac{\hat{r}_m \cdot \vec{l}_{mn}}{|\vec{l}_{mn}|}\right) \quad (4)$$

where a_m is the total fixed amplitude offset (due to line attenuation, mismatch, gain, and so on) in antenna m, $D_m(\theta)$ is the directivity of antenna m for an angle θ relative to broadside, $\vec{l}_{mn}$ is the vector pointing from the phase center of antenna i to the phase center of antenna n, ϕ_m is the total fixed phase offset in antenna m, and $\hat{r}_m$ is the unit vector normal to the surface of the array, which describes the orientation of

---

[3]The model for a 2-D phased array is very similar and involves only changing the directivity function to a function of two variables (i.e., $D_i(\theta_{mn}, \varphi_{mn})$): the azimuth and elevation angles between elements m and n.
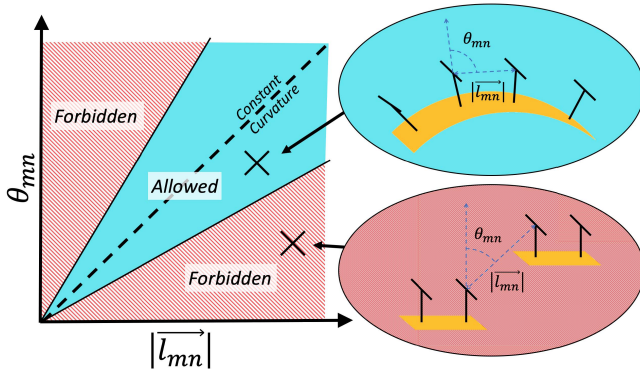
Fig. 5. Visualization of forbidden and allowed regions of the $\theta_{mn} \otimes |\vec{l_{mn}}|$ vector space for physically restricted phase arrays. The "constant curvature" line is shown in dashed blue in the center of the allowed region. We also illustrate an example of a shape that generates an allowed $\{\theta_{mn}, |\vec{l_{mn}}|\}$ pair (top right) and a forbidden $\{\theta_{mn}, |\vec{l_{mn}}|\}$ pair (bottom right). As we can see, the forbidden $\{\theta_{mn}, |\vec{l_{mn}}|\}$ pair can only be generated if the array is cut in half.

antenna m. We take $D_m(\theta = 0) = 1$ for all m's. We assume no significant angle dependence for the phase response of the antenna.

As is evident, there are amplitude and phase offset terms that can prevent us from drawing a bijection between coupling and distance. To isolate the distance terms, we perform a one-time calibration of the array in the completely flat configuration. The information gathered during this measurement is another coupling matrix, S^{flat}:

$$S_{mn}^{\text{flat}} = \frac{a_m D_m(\theta_{mn}^{\text{flat}}) a_n D_n(\theta_{nm}^{\text{flat}})}{|\vec{l_{mn}^{\text{flat}}}|} e^{-j\left(\phi_m + \phi_n + k\left|\vec{l_{mn}^{\text{flat}}}\right|\right)}. \quad (5)$$

Because the geometry of the flat configuration is fixed and known, we can make some basic assumptions to simplify the model for flat coupling. First, in a flat array, $\theta_{mn}^{\text{flat}} = (\pi/2)$ when $m \neq n$. Moreover, assuming that our array is composed of identical antennas, $D_n(\theta) = D_m(\theta) = D(\theta)$ for all m's and n's. Thus, we can simplify our flat coupling model to

$$S_{mn}^{\text{flat}} \cong \frac{a_m a_n D\left(\frac{\pi}{2}\right)^2}{|\vec{l_{mn}^{\text{flat}}}|} e^{-j\left(\phi_m + \phi_n + k\left|\vec{l_{mn}^{\text{flat}}}\right|\right)}. \quad (6)$$

Moreover, $|\vec{l_{mn}^{\text{flat}}}|$ is known in advance. To eliminate the fixed power and phase offsets, we define the normalized transfer function, H

$$H_{mn} \equiv \frac{S_{mn}}{S_{mn}^{\text{flat}}} \quad (7)$$

$$= \frac{D(\theta_{mn}) D(\theta_{nm})}{D\left(\frac{\pi}{2}\right)^2} \frac{|\vec{l_{mn}^{\text{flat}}}|}{|\vec{l_{mn}}|} e^{-jk\left(\left|\vec{l_{mn}}\right| - \left|\vec{l_{mn}^{\text{flat}}}\right|\right)}. \quad (8)$$

B. Constant Curvature Assumption

The dependence of the transfer function, H, on the angle matrix, θ, presents a complication. Angles θ_{mn} and θ_{nm} are two *additional* degrees of freedom, theoretically independent of $|\vec{l_{mn}}|$, which presents a challenge to finding a bijection between coupling and distance. In the case of two mechanically detached radiators, each of the three variables $|\vec{l_{mn}}|$, θ_{mn}, and θ_{nm} can induce changes in the coupling independently.

However, because our radiators are fixed to a nonstretchable ground plane,[4] mechanical constraints in this system reduce the allowable space of parameters from all of $\mathbb{R}^3$ to a smaller subspace in $\mathbb{R}^3$. To illustrate this, let us consider the special 2-D case of only $|\vec{l_{mn}}|$ and θ_{mn}; the mechanical constraint has the effect of partitioning $\mathbb{R}^2$ into "forbidden" and "allowed" subspaces, where pairs of $\{|\vec{l_{mn}}|, \theta_{mn}\}$ in the "forbidden" subspace are incompatible with the mechanical constraint, as illustrated in Fig. 5. The "allowed" pairs occupy a subspace in the shape of a triangular wedge: for some distances, the angular freedom is highly restricted and for other distances, the angular freedom is large.[5]

There are multiple methods of dealing with the problem of optimizing over a high-dimensional space while respecting the mechanical constraints at play. One is to computationally simulate the array and generate the $\{|\vec{l_{mn}}|, \theta_{mn}, \theta_{nm}\}$ triplets through brute force. Another is to attempt to characterize this subspace analytically. Finally, we have the option of assuming this subspace is very thin and treating it as a line. This third option is equivalent to assuming that the array ground plane only takes on shapes of constant curvature, and this is the option we elect to use for the purposes of this article.[6] This is reasonable, as, in the most practical case, where the surface bends smoothly without sharp kinks, the local curvature in a small neighborhood of several adjacent antennas can be considered constant. This allows our approach to be applied locally even for nonconstant curvature cases.

Furthermore, the signal-to-noise ratio (SNR) of measurements between elements that are far apart, with many intervening elements, is lower than elements within a smaller neighborhood (due to occlusion, reflections, attenuation, and so on) and do not contribute a great deal to the overall quality of the shape reconstruction.[7] As we will see in Section IV, coupling measurements between far apart elements have a diminishing impact on shape reconstruction, and thus, it is not necessarily important how we model them.

Using the constant local curvature assumption, we have reduced the space of independent variables to $\mathbb{R}^1$ and have, thus, found a bijection between θ_{mn} and $|\vec{l_{mn}}|$. This implies that we can replace our angle-dependent directivity, $D(\theta_{mn}(|\vec{l_{mn}}|))$,

---

[4]Even a stretchable ground plane places restrictions on antenna mobility and introduces a mechanical constraint that reduces the allowable space of independent variables, though to a lesser degree.

[5]Two caveats about the exact visualization presented;

1) This plot looks different for different antenna pairs and is characterized by $|\vec{l_{mn}^{\text{flat}}}|$.
2) The exact appearance presented here is inaccurate: the allowed region may not grow positively with increasing distance. The constant curvature assumption is not guaranteed to be a line. The space may not be symmetric.

[6]It should be noted that the general framework presented so far does not depend on this assumption, and implementations of the first two options are certainly possible.

[7]This assumption does not preclude an ability to reconstruct the shape of phased array systems with large numbers of elements. We can instruct our algorithm to only measure and model local measurements, which can each have a different curvature. Although, for each small neighborhood of antennas, a constant local curvature is assumed, the curvature for an adjacent (and possibly overlapping set) can be different, leaving open the possibility for a shape with varying curvature.
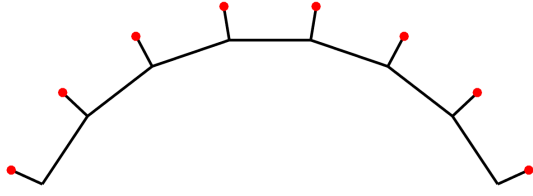
Fig. 6. Side view of a flexible phased array (f = 2.5 GHz, 0.6λ antenna spacing, and quarter-wave dipole antennas) with constant curvature, $R = -0.222$ m. Ground plane and dipole feed are in black and antennas in red.

with a distance-dependent directivity, $D(|\vec{l_{mn}}|)$. This simplifies our transfer function model to

$$H_{mn} = \frac{D(|\vec{l_{mn}}|)^2}{D(|\vec{l_{mn}^{\text{flat}}}|)^2} \frac{|\vec{l_{mn}^{\text{flat}}}|}{|\vec{l_{mn}}|} e^{-jk\left(|\vec{l_{mn}}|-|\vec{l_{mn}^{\text{flat}}}|\right)}. \tag{9}$$

We choose to determine the relationship between θ_{mn} and $|\vec{l_{mn}}|$ computationally; we begin by geometric modeling of the array. An example of the array model with a constant radius of curvature is shown in Fig. 6, where a 2.5-GHz flexible phased array with 0.6λ antenna spacing and dipoles antennas that extend 0.25λ normal to the local ground plane is shown.

We iterate over a large number of radii of curvature,[8] where $R < 0$ corresponds to convex array orientation and $R > 0$ to concave array orientation. At each iteration, we generate one-to-one mappings $R \xrightarrow{\aleph} |\vec{l_{mn}}|$ and $R \xrightarrow{\beth} \theta_{mn}$. To generate our bijection, we simply invert $\aleph$

$$\theta_{mn}\left(|\vec{l_{mn}}|\right) = \beth\left(\aleph^{-1}\left(|\vec{l_{mn}}|\right)\right). \tag{10}$$

Practically, this is implemented simply as a vector of θ_{mn} and a vector $|\vec{l_{mn}}|$, which are paired and correspond to a vector of curvature radii.

We now have a bijection between distance and angle, pushing us one step closer to incorporating directivity in our model. To quantify directivity, there are a number of options: analytical antenna model, simulated directivity pattern, and direct measured results. Any of these options yields a function $D(\theta)$, which completes our model for the transfer function, H.

C. Iterative Spiral Match

Armed with a model that draws a bijection between mutual coupling and distance, we can theoretically execute Spiral Match. The Euclidean distance between the elements m and n, as defined by (1), can be estimated by minimizing the magnitude of the difference between the measured transfer function, $H_{mn}^{\text{meas}} = S_{mn}^{\text{meas, bent}} / S_{mn}^{\text{meas, flat}}$, and the estimate of (9)

$$E_{mn} = \left(\underset{|\vec{l_{mn}}| \in [d_{mn}^{\min}, d_{mn}^{\max}]}{\arg\min} \left|H_{mn}^{\text{meas}} - H_{mn}(|\vec{l_{mn}}|)\right|\right)^2 \tag{11}$$

where $d_{mn}^{\min}$ and $d_{mn}^{\max}$ are the minimum and maximum physically possible distances for the antenna pair. This can be envisioned as the projection of the measurement H_{mn}^{meas} onto
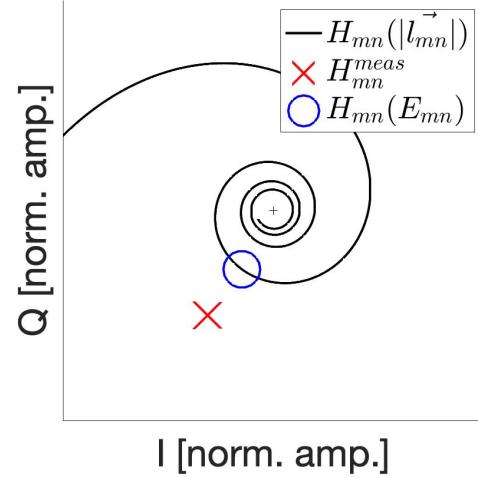
[8]In this example, $R \in \pm[0.025, 1]$ m.

Fig. 7. Visualization of the Spiral Match algorithm. In black, the coupling transfer function model, $H_{mn}(|\vec{l_{mn}}|)$, for variable distance is given. The red "X" is our measured coupling, H_{mn}^{meas}. It is "projected" onto the model via the argmin function to give us the blue circle, which is the position on the model that corresponds to our predicted distance, E_{mn}.

the closest location on a spiral generated by H_{mn}, as shown in Fig. 7, and is the essence of Spiral Match. This location corresponds to the predicted distance, $|\vec{l_{mn}}|$. Unfortunately, because of measurement noise and imperfection, solving for the Euclidean distance in a single step leads to errors, which can result in potentially nonphysical solutions.

The single-step Spiral Match projection is prone to issues in the presence of nonline-of-sight (NLOS) element coupling for convex configuration, where NLOS and surface-mode coupling can dominate. In this case, power changes do not follow the simple directivity model. In addition, amplitude ambiguity at a given phase for an imperfect measurement can lead to erroneous projection of the measurement onto an incorrect segment of the spiral (introducing distance error on the order of λ).

Small distance error is acceptable and can potentially be fixed in the second step of our framework semidefinite relation (SDR); large distance error, however, often makes SDR unworkable and results in a completely erroneous shape prediction. Mitigating large distance error is the intention of the iteration process discussed in the following.

To mitigate these issues, we invoke Spiral Match in a number of iterations, each time adding more constraints to the system to help ensure the accuracy of the predicted Euclidean distance. These iterations and the associated constraints are shown in I. In the first iteration, we assume no curvature polarity (concave/convex) to minimize constraints on the problem. Without a polarity, we make no assumption of the geometry and, thus, *do not* include directivity in the model. For the first pass, we assume that $D(|\vec{l_{mn}}|) = 1 \forall i, |\vec{l_{mn}}|$ and use the optimization function in 11 to compute the first prediction of the EDM, E^1. The result of this first iteration is a very crude prediction of Euclidean distance that is sufficiently accurate to determine the polarity of the shape. The polarity $p \in \{-1, +1\}$ (-1 being convex and $+1$ being concave) is decided using a

TABLE I
ITERATIONS OF SPIRAL MATCH

Iteration #	Constraint(s)	Action	Result	Calculation	Output
1	-	-	E^1	Calculate polarity	Polarity
2	Polarity	Add directivity if concave	E^2	Run RWC	Phase wrap matrix
3	Polarity, Phase wrap matrix	Restrict distance search space	E^3	-	-

voting scheme[9]

$$ p = \text{sign}\left(\sum_{i \neq j} \text{sign}\left(\left| \vec{l}_{mn}^{\,\text{flat}} \right| - E_{mn}^1 \right) \right). \qquad (12) $$

In the second iteration, we use p to inform whether or not to include directivity in the coupling model. The second prediction of the EDM, E^2, is computed using the optimization function in (11). Having eliminated ambiguity about polarity and including the directivity for concave shapes, we can turn our attention to the problem of phase wrapping-induced distance error. These errors are on the order of λ, which is often large enough to violate physical constraints, and so it becomes germane to develop such a solution that will intelligently identify violations. We call it "recursive wrap correction" (RWC).

RWC, the details for which are provided in Appendix A, is an algorithm that converts a matrix of integers, $R \in \mathbb{Z}^2$, representing the number of complete phase wraps associated with the distances in E^2, to a "corrected" phase wrap matrix, R'. It can also correct for outlier measurements not caused by phase-wrapping that may carry large distance error.

In the third iteration of the Spiral Match algorithm, the search space for distance is truncated to a single one-wavelength range as follows:

$$ \left| \vec{l}_{mn} \right| \in \left[R'_{mn}\lambda, (R'_{mn} + 1)\lambda \right) \qquad (13) $$

to ensure that all predicted distances have the same number of wraps as RWC predicted. If R' is correct, this has the effect of ensuring that there are no phase wrapping-induced distance errors, which improves Spiral Match's accuracy. Spiral Match culminates with a final minimization, using the reduced search space

$$ E_{mn}^3 = \left(\underset{\left| \vec{l}_{mn} \right| \in \left[R'_{mn}\lambda, (R'_{mn}+1)\lambda \right)}{\arg\min} \left| H_{mn}^{\text{meas}} - H_{mn}\left(\left| \vec{l}_{mn} \right| \right) \right| \right)^2. \qquad (14) $$

At this point, it is unlikely that E^3 is perfectly symmetric. This is acceptable for the purposes of the next step—ASC—but it can be advantageous because we have two candidates for distance for each element pair. We can leverage this advantage by finding some metric to compare these two, and opting to

use the better one. An obvious candidate for this metric is the "projection error," ΔH, defined as

$$ \Delta H_{mn} = \min_{\left| \vec{l}_{mn} \right| \in \left[R'_{mn}\lambda, (R'_{mn}+1)\lambda \right)} \left| H_{mn}^{\text{meas}} - H_{mn}\left(\left| \vec{l}_{mn} \right| \right) \right| \quad (15) $$

which corresponds to the distance in the complex plane between the measurement and the model at the predicted point, E_{mn}^3. A large projection error is an indication that the model does not possess a complex value close to the measurement—implying large measurement error. However, this implication only holds some of the time; we have observed that this correlation between prediction error and projection error occurs for the patch antennas discussed below, but not for the dipole antennas. Because this is another "switch," we can elect to turn flip it or not. To "flip it," we force the EDM to be symmetric using the projection error as the deciding metric

$$ E_{mn}^{3'} = \begin{cases} E_{mn}^3 & \Delta H_{mn} \leq \Delta H_{nm} \\ E_{nm}^3 & \Delta H_{mn} > \Delta H_{nm} \end{cases} \qquad (16) $$

where $E^{3'}$ is the symmetrized version of E^3. E^3 (or $E^{3'}$) is the input to the second phase of the shape reconstruction framework algorithm, as discussed in the following.

IV. CANDIDATE FOR ASC: SEMIDEFINITE RELAXATION

Using a prediction of the EDM corresponding to antenna phase centers on a flexible phased array, E^3, we can solve the problem of reconstructing relative position or shape. Like many other high-dimensional problems, this can be solved with a single eigenvalue decomposition [26]. Solving the position problem with an EDM in this way is called "Classical Multidimensional Scaling" (MDS), which involves few matrix operations. MDS, simple as it is, typically fails for imperfect EDMs. If, for example, $E_{mn} = |r_i - r_j|^2 + \alpha_{mn}$, where α_{mn} is some noise-adding term, our eigenvalue decomposition may yield complex (i.e., nonphysical) eigenvalues. In addition, sparse or mislabeled EDMs cannot be used with MDS. A number of algorithms have been written and studied for different purposes and qualify as candidates for the second transformation, ASC [26].

In this system, we do not suffer from sparse or mislabeled EDMs and choose to use semidefinite relaxation (SDR)[10] as the candidate for ASC, for the following reasons.

1) SDR offers the option to use a mask matrix W to weight elements in the EDM individually. This allows us to

---

[9]$N^2 - N$ pairs are an even number, and it is possible that $p = 0$. If this happens, it is likely because $|\vec{l}_{mn}^{\,\text{flat}}| - E_{mn}^1 \approx 0$, and a small degree of error in E_{mn}^1 is pushing the difference above and below zero for different (i, j). In this case, the array is likely in a flat or an approximately flat shape, and the choice of polarity is almost irrelevant. In the algorithm, we overwrite $p = 0$ cases to have $p = +1$ for these incredibly rare circumstances.

[10]We implemented SDR as recommended in [26]—written in MAT-LAB using "cvx," a framework for performing convex optimization in MATLAB [28].

TABLE II
EDM MASK MATRIX STRUCTURE CANDIDATES

Type	Equation	Knob(s)
Uniform	$W_{mn} = 1$	-
Binary	$W_{mn} = \begin{cases} 1 & |m-n| < a \\ 0 & |m-n| \geq a \end{cases}$	a
Linear	$W_{mn} = a|m-n| + b$	a, b
Quadratic	$W_{mn} = a|m-n|^2 + b|m-n| + c$	a, b, c
Exponential	$W_{mn} = a^{-b|m-n|} + c$	a, b, c

control how much each EDM entry "matters." Because local coupling measurements have higher quality than distant measurements, we want to be able to weigh local measurements more.

2) SDR searches a much smaller, convex vector space and, thus, guarantees a physical result while also decreasing runtime.

3) SDR showed the best performance along with multiple metrics in [26].

The option to use a mask matrix W to window entries that have not been collected (i.e., in mic/speaker localization in a large theater) is an option that allows us to use this method for large array systems or ones where some elements have only either a receiver or a transmitter. In this work, we collect a completely dense EDM, and we use a mask matrix to weight entries based on SNR.

Recognizing that $\text{SNR}(S_{mn}) \propto \frac{1}{|\vec{l_{mn}}|^2}$, it is likely that the EDM error, δE, defined as

$$\delta E_{mn} = \left| |\vec{l_{mn}}| - E_{mn}^3 \right| \qquad (17)$$

follows the general trend

$$\delta E_{mn} \propto \left| \vec{l_{mn}^{\text{flat}}} \right|^k \qquad (18)$$

where k is some unknown exponent. We can leverage this known relationship by weighting higher quality EDM entries more than lower quality ones. The intuitive approach to implement this is to have entries in matrix W decrease as we move away from the diagonal.

We have the freedom to design W as we choose, based on the system, to minimize shape reconstruction error. We have explored a number of structures for W, some of which are presented in Table II. In most of these structures, we have a design "knob" that can be turned to adjust for different systems and optimized to minimize shape reconstruction error. We have found the best performance with a mask matrix where entries are uniform for close pairs and exponential for far pairs.

V. PASSIVE FLEXIBLE PHASED ARRAYS

A. Test Apparatus

In order to validate the proposed shape reconstruction method, we built several connectorized flexible phased arrays. While lacking the dynamic, multipurpose capabilities of an integrated flexible phased array, connectorized arrays allow for quick measurements of mutual coupling (e.g., by a standard
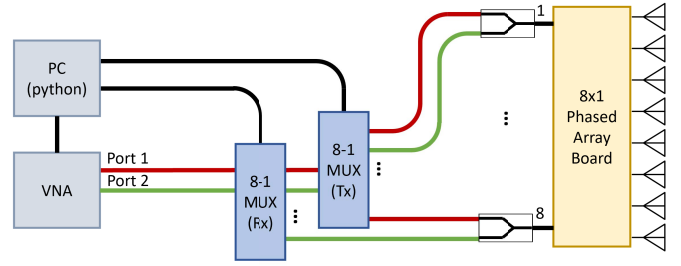

Fig. 8. Test setup for coupling measurements of connectorized arrays.
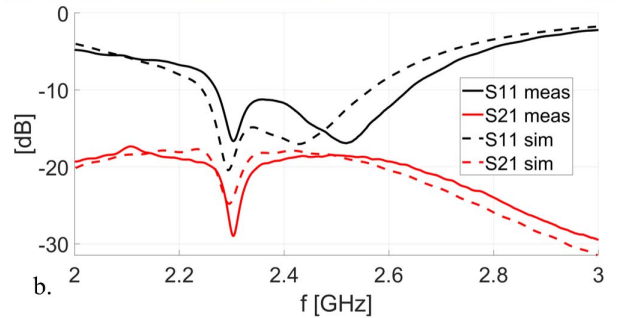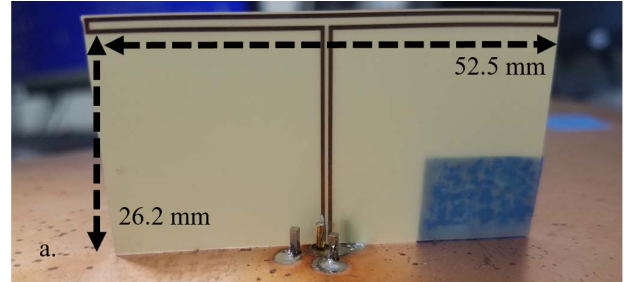

Fig. 9. (a) Folded dipole antenna design dimensions. (b) Measured and simulated folded dipole input matching and adjacent element coupling.

vector network analyzer). The connectorized array elements are designed to have center frequencies close to 2.5 GHz with an element pitch of 0.6λ. Results from eight-element, 1-D arrays with folded dipole and patch antennas are presented in the following.

A block diagram of the measurement setup of a connectorized array on the rigid frame is depicted in Fig. 8. In order to measure the full coupling matrix of the array without changing connectors, each element connects to an RF splitter then two digitally controlled 8-to-1 RF multiplexers that are then connected to the ports of a vector network analyzer. A computer and script control the multiplexers, trigger the VNA, and log the coupling measurements. To flex the connectorized arrays into known shapes in a quick and repeatable fashion, rigid wooden frames of known convex and concave bend radii were designed and built. These frames are shown in the first column of Fig. 12.

B. Folded Dipole Array Results

The folded dipole used in the measurements is shown in Fig. 9. Ground plane-backed dipoles (folded or unfolded) are well suited to mutual coupling shape reconstruction. Radiation from a dipole originates from the current distribution on the arms and is initially omnidirectional (except for the
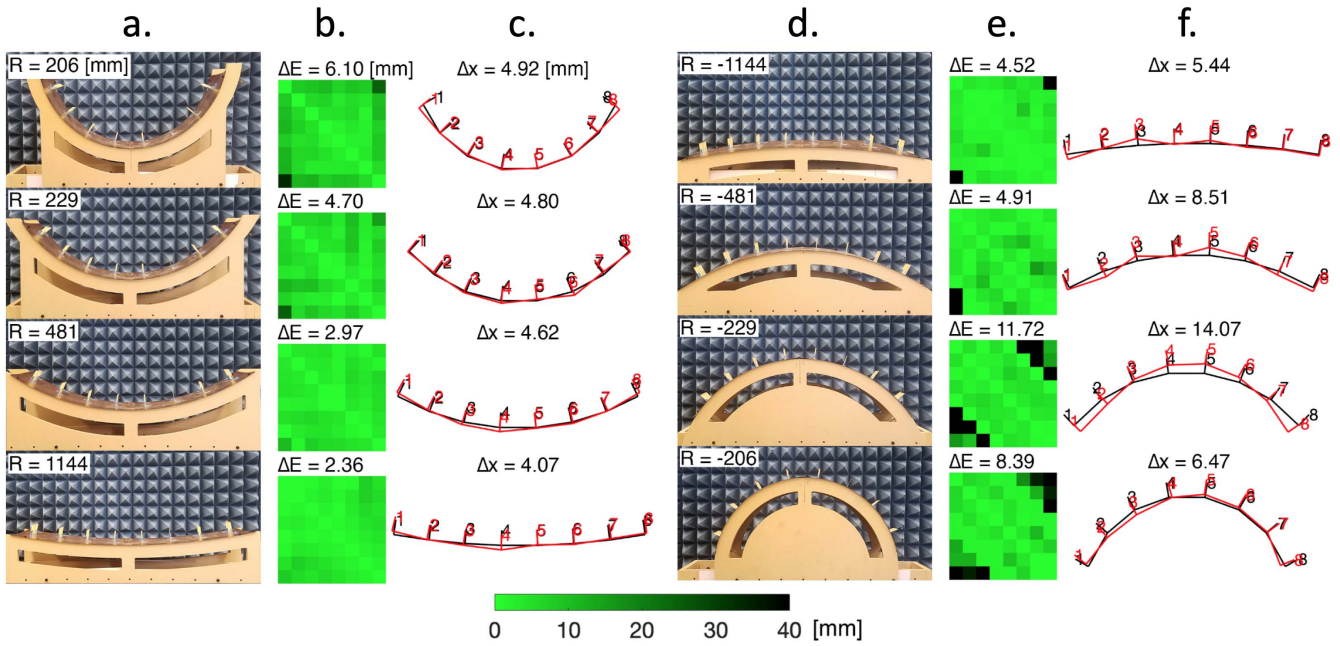
Fig. 10. Shape reconstruction results for passive 2.5-GHz folded dipole phased arrays. (a) Concave wooden frames with dipole antennas and curvature radii. (b) EDM error heatmaps and mean EDM error (ΔE) for concave shapes. (c) Reconstructed antenna shapes (red), true antenna shapes (black), and mean shape error (Δx) for concave shapes. (d) Convex wooden frames with dipole antennas and curvature radii. (f) EDM error heatmaps and mean EDM error (ΔE) for convex shapes. (f) Reconstructed antenna shapes (red), true antenna shapes (black), and mean shape error (Δx) for convex shapes.

direction along the arms themselves) prior to reflection off of the ground plane. Because this omnidirectional radiation originates well above the ground plane, the coupling is less sensitive to occlusion and has propagation properties close to the ideal far-field assumed by our simplified propagation model. The folded dipole presents an input impedance of 275 Ω at its arms. A high-impedance edge-coupled quarter-wave transmission line extends to the ground plane, transforming the antenna input impedance and connecting to a 50-Ω SMA connector.

The folded dipole array shape reconstruction results are shown in Fig. 10. The far-field radiation pattern used in the algorithm was determined using a finite-difference time-domain (FDTD) simulator. The accuracy of Spiral Match is measured by ΔE, the mean element pair distance error. ΔE is the mean difference between the predicted distances and the "truth" distance predicted by the known physical design dimensions of the frames. The accuracy of the shape reconstruction is measured by Δx, which is the mean difference between the reconstructed element position and the position of the elements according to the frame design dimensions. An exponential weighting matrix was used within the semidefinite relaxation algorithm.

C. Patch Antenna Array Results

The next array used for testing the shape reconstruction algorithm is an eight-element linearly polarized patch antenna array. While the folded dipole antennas are near ideal candidates for shape reconstruction, patch antennas present a greater challenge. The challenges offered by patch antennas are a bellwether for if shape reconstruction could be a ubiquitous tool for a wide variety of flexible arrays or is limited to
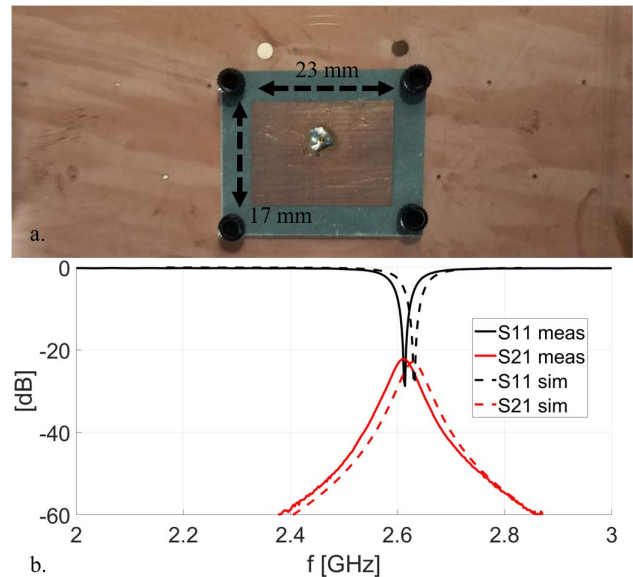

Fig. 11. (a) Patch antenna design dimensions. The substrate extends 5 mm around the copper patch. (b) Measured and simulated patch antenna input matching and adjacent element coupling.

a narrow subset of ideal systems. Typical patch antennas are low profile, highly resonant, and inherently directional with radiation emerging from fields located at both ends of the patch along its excitation axis (E-field line). In a flexible array, their low profile means that they are more susceptible to occlusion and do not share the pseudoomnidirectionality of the ground plane backed dipoles. The highly resonant nature (particularly when built on thin substrates) leads to low matching bandwidth. Low matching bandwidth can affect the quality of coupling measurements as a pair of
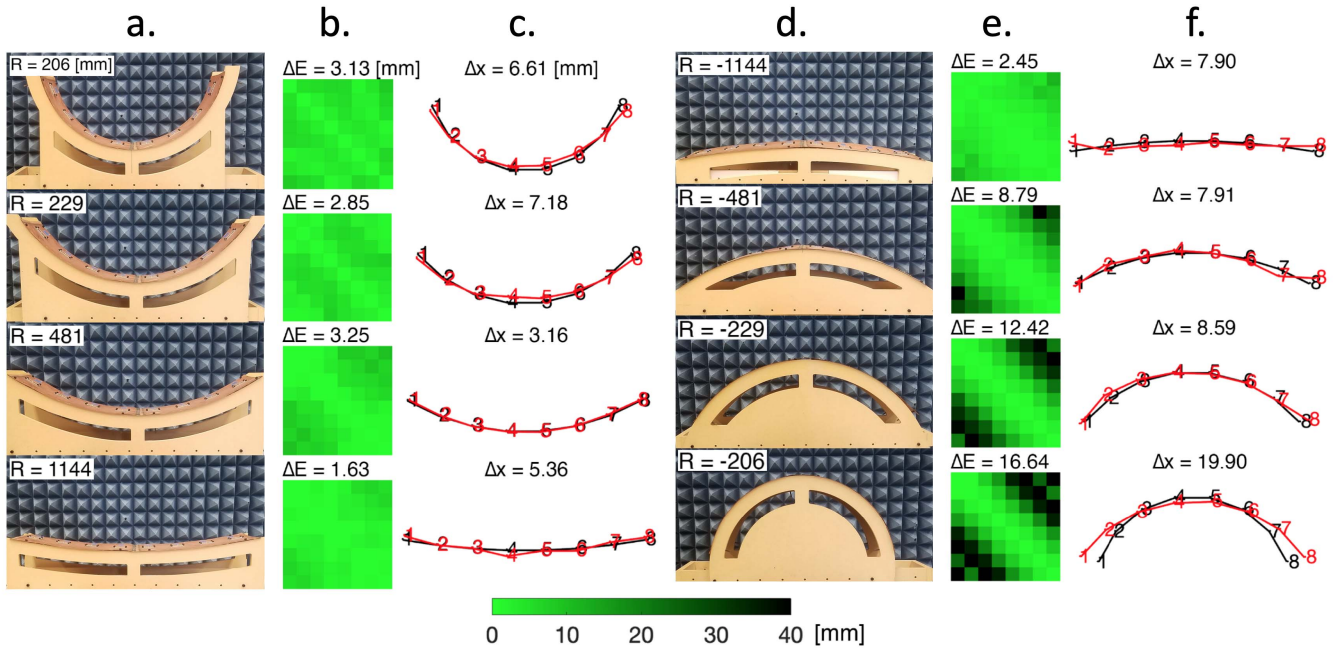
Fig. 12. Shape reconstruction results for passive 2.5-GHz patch antenna phased arrays. (a) Concave wooden frames with patch antennas and curvature radii. (b) EDM error heatmaps and mean EDM error (ΔE) for concave shapes. (c) Reconstructed antenna shapes (red), true antenna shapes (black), and mean shape error (Δx) for concave shapes. (d) Convex wooden frames with patch antennas and curvature radii. (e) EDM error heatmaps and mean EDM error (ΔE) for convex shapes. (f) Reconstructed antenna shapes (red), true antenna shapes (black), and mean shape error (Δx) for convex shapes.

patches could de-tune from each other as the array changes shape.

The presented patch antenna, as depicted in Fig. 11, is made with the 1.27-mm-thick high dielectric substrate (ϵ_r 11.2) in order to reduce their size and better facilitate bending. The feed is inset by 6.35 mm in order to match to 50 Ω. The far-field radiation pattern used in the algorithm was determined using an FDTD simulator. The results of the patch antenna shape reconstruction are shown in Fig. 12. The patch antennas shape reconstruction is as accurate as the dipole reconstruction with the exception of the most convex shape. The final matrix in Fig. 12 shows higher error in the off-diagonal element pair distances, which would indicate that occlusion caused by the extreme bend is the culprit. Despite this, the results show the viability of the shape reconstruction algorithm for radiator with the tightly confined near-field profile.

VI. ACTIVE INTEGRATED FLEXIBLE PHASED ARRAY

A. Array Design

While the passive, connectorized arrays presented above are useful tools for understanding mutual coupling shape reconstruction, they do not provide the utility of a fully integrated flexible phased array. A truly self-contained flexible phased array is enabled by RFICs, which combines array element functions (frequency synthesis, phase shifting, power amplification, and so on) in a compact and low-profile package. Conventional silicon ICs are rigid but are sufficiently small as to not significantly change the flexibility of a larger flexible phased array. An integrated circuit flexible phased array prototype was created to demonstrate mutual coupling shape calibration and reconstruction. The implemented array

is a 1-D, eight-element transmit and receive capable array operating at 10 GHz built on a four-layer flexible printed circuit board (PCB), as presented in [21] and shown in Fig. 13. The circuit and radiator subcomponents are briefly described below.

1) Element Circuit: Each element circuit consists of a custom single-channel transmitter/receiver integrated circuit, which is implemented in a standard 65-nm CMOS process.

The RF path of the RFIC starts with a 2.5-GHz phase reference signal, which is shared by all elements in the array. The phase reference is used by the phase-locked loop (PLL) to synthesize 10-GHz IQ signals. The PLL uses programmable divider current injection to provide 360°+ phase control to its output, which is fed to both the transmit and receive paths. An SPI digital interface controls all programmable subcircuits. In the transmit path, the signal passes through a programmable IQ summation phase shifter, which provides another independent 360° phase control. The phase shifter is controlled by a programmable SRAM, allowing for rapid phase shifting for beam steering or data modulation. The phase shifter can be disabled and bypassed to reduce power consumption. With the PLL phase control and the IQ summer, the transmit and receive phases can be set arbitrarily and independently. The transmit path ends in a power amplifier (PA) and balun before the signal is sent off-chip to the radiator.

The receive path begins at the same balun that the PA is driving. A receive-enable switch between one side of the balun and ground allows the receiver to measure the PA output (switch closed) and allows the receiver to see higher impedance when the PA is not operating (switch open). A bypass-able amplifier ensures that the receive channel has sufficient dynamic range to measure small signals and the large
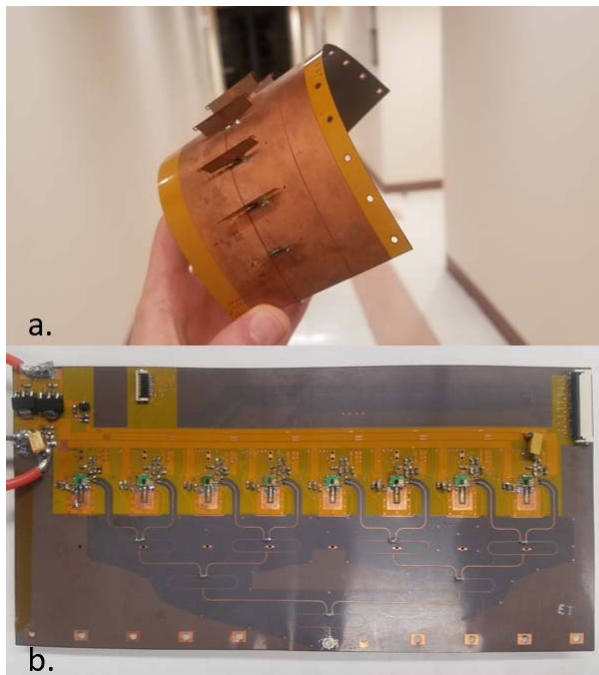
Fig. 13. (a) Integrated circuit-based flexible phased array with eight elements bent in hand with front shown. (b) Array back with feed network, chips, interposers, and circuitry shown.
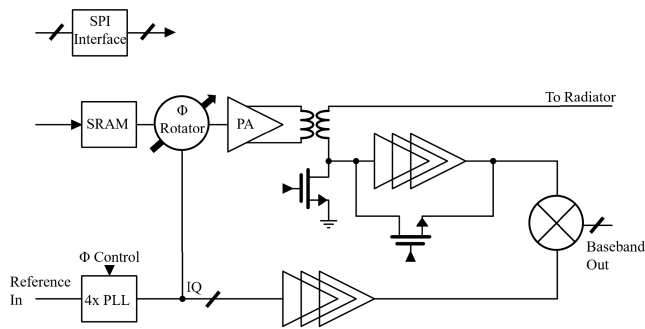

Fig. 14. Custom RFIC element circuit block diagram.

Fig. 15. (a) RFIC die photograph. (b) Interposer with RFIC. (c) Three interposers mounted on flexible PCB.

signals from self-loop or adjacent element measurements. This amplifier is followed by a direct down-conversion IQ mixer. The resulting baseband IQ signals are digitized and processed off-chip.

Each element RFIC is mounted on a thin two-layer interposer made from a traditional RF PCB substrate. While PCB substrates are rigid when thick, a small, thin interposer does not affect the flexibility of the larger board. The supply filtering capacitors are aligned with the axis of bending to minimize their effect on overall stiffness, ensuring that the bend radius is limited by the plastic deformation of the flexible PCB. The block diagram is shown in Fig. 14, and RFIC die photograph and interposer are shown in Fig. 15.

2) Radiator: The radiator, built from a single sheet of copper on polyimide, is a ground plane backed dipole. By aligning the dipole arms with the axis of bending, the array can be flexed significantly without strongly affecting radiator performance. In addition to having favorable properties for shape reconstruction, ground plane backed dipoles provide the wide, single-lobe pattern that is desirable for beam-steering
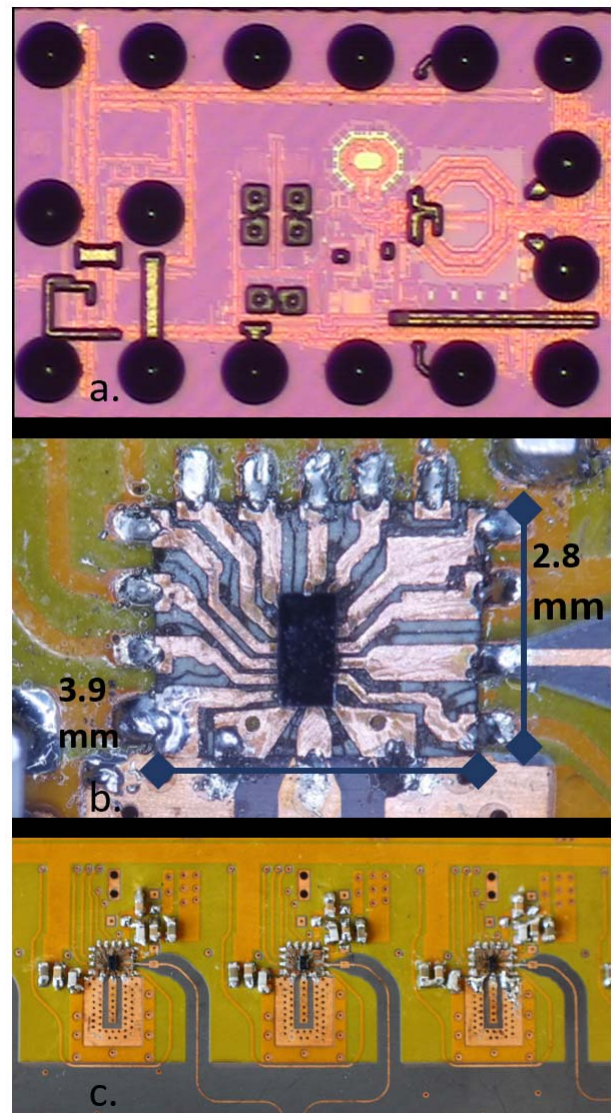
applications. The radiator, as shown in Fig. 16(a), is mounted perpendicular to the surface of the ground plane, which avoids the need for a thick, likely rigid, layer of the substrate. Element pitch is 0.6λ. The measured and simulated far-field patterns with and without bending are shown in Fig. 16(b) and (c). One leg of the radiator connects to a single-ended transmission line, while the other is grounded. The vertical feed acts as a balun to convert the input to a differential drive for the radiating arms. The residual asymmetry is observed in Fig. 16(b) as the pattern tilts slightly toward the grounded leg. Overall, the simulated, flat, and bent results match closely. The deviation between bent and flat performance is present in the $\phi = 90°$ cut where the bent result experiences slightly less lobe splitting than the flat simulated and measured results. This is consistent with the expectation that a convex bend increases element spacing, decreasing the interelement coupling, which contributes to lobe splitting. This pattern change with the array shape is small and does not meaningfully affect the quality of the shape reconstruction results.
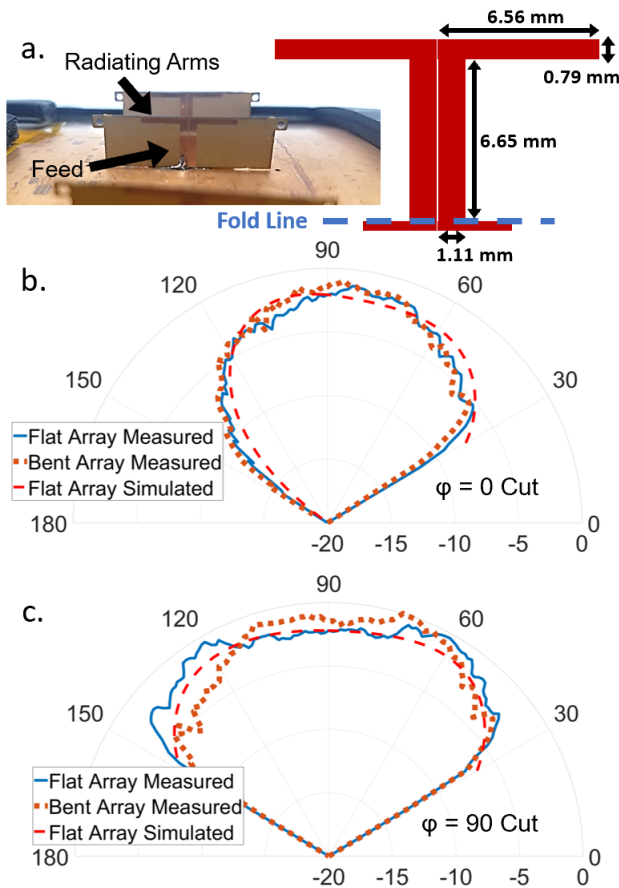
Fig. 16. Element radiator. (a) Radiators mounted on flexible PCB and radiator dimensions. The feet beneath the fold line are soldered to the circuit board. (b) Measured and simulated in-array element patterns for $\varphi = 0°$ cut. Pattern is measured flat and when the array is conformed to a 120-mm convex bend radius. (c) Measured and simulated in-array element patterns for $\varphi = 90°$ cut. All measurements are normalized to their global maximum.

B. Active Integrated Flexible Phased Array Shape Reconstruction

Shape reconstruction using the flexible integrated circuit-based phased array is demonstrated in Fig. 17. Eight rigid frames ($R = \pm100, 150, 220, 400$ mm) were used to provide repeatable reference dimensions. The on-chip PAs and receivers were used to collect the coupling measurements. When adjusted by a factor of four to account for wavelength difference between 2.5 and 10 GHz, the final shape error, Δx, outperforms the connectorized 2.5-GHz dipole array. The minimum, maximum, and average Δx's are lower. While some of this performance increase can be contributed to a smaller ratio of bend radii to array length, it shows the viability of shape reconstruction in integrated circuit arrays. The shape reconstruction framework is shown to be frequency agnostic by these results. While the framework itself is agnostic, there are practical concerns for which frequency is involved. The 10-GHz array is smaller, as such nearby objects and reflectors are relatively farther away and less likely to affect local coupling measurements through reflections. As such, the higher frequency may be responsible for the more accurate results. Improved quality of coupling
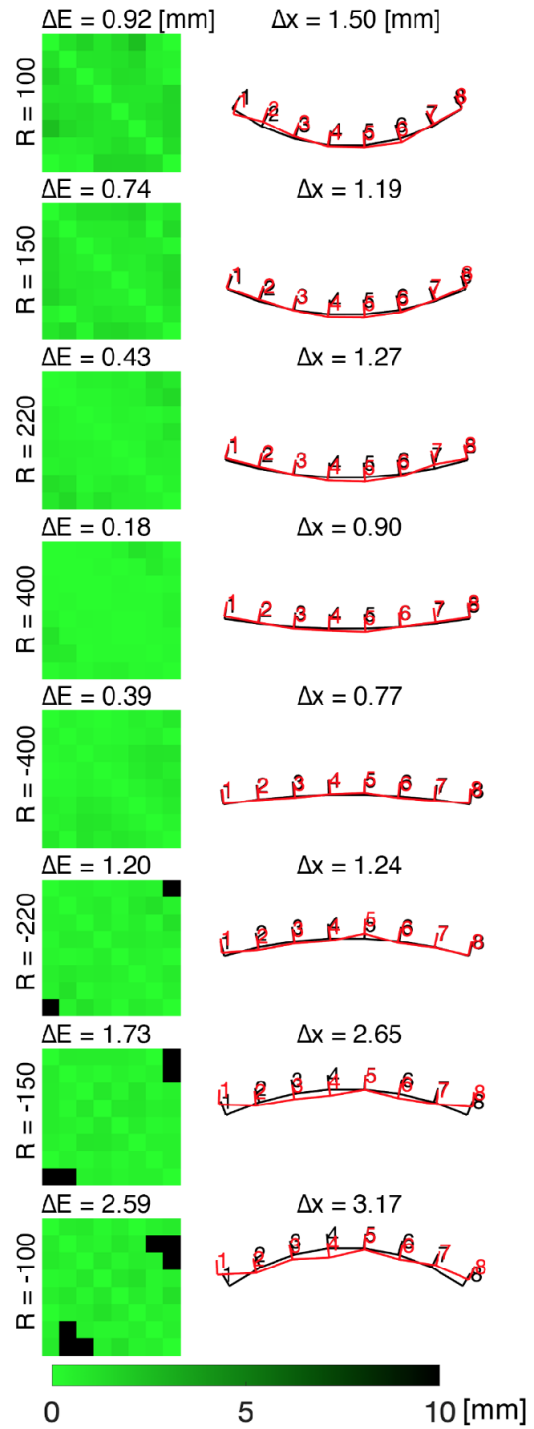

Fig. 17. Shape reconstruction results for integrated 10-GHz phased arrays with dipole antennas for various radii of curvature. Left: EDM error heatmaps and error mean (ΔE). Right: reconstructed antenna shapes (red), true antenna shapes (black), and shape error mean (Δx).

measurements does come with a mechanical tradeoff. As the operation frequency of the array rises, its flexibility could decrease as the density of rigid or semirigid components, and the complexity and thickness of signal routing increase with finer antenna pitch.

VII. GENERALIZING FOR OTHER SYSTEMS

The framework presented in this work is multistaged and multifaceted, offering many opportunities for modification and

expansion. In this section, we will revisit how this framework can easily be implemented when other antennas, sizes, or array constraints are in use.

Our choice of EDMs as a physical constraint is a convenient (perhaps obvious) one but by no means the only one. A system that has other sensors or capabilities can easily accommodate an algorithm relying on angle or curvature as the constraint. Choosing another physical constraint necessitates modifications to or alternatives for PCM and ASC as well.

Spiral Match (the PCM algorithm in our implementation) is rooted in a model for the coupling—this model can easily be changed to include other constraints or known EM phenomena to improve its versatility and accuracy. We used our simplified model to predict the Euclidean distance in three iterations, but, again, these iterations and the constraints they leveraged were system-dependent. Additional iterations can be added if a system is more or less constrained. Moreover, the parameters of our iterations can be easily changed for new systems. For example, the constraints used in the RWC algorithm can be easily changed.

New candidates for PCM could leverage frequency diversity if the system included broadband antennas. While broadband systems *could* use the single frequency approach presented in this work, frequency diversity would alleviate phase wrapping ambiguity when determining distance. Mutual coupling could be measured at multiple frequencies or using a chirp similar to frequency-modulated continuous-wave (FMCW) radar from which a distance matrix would then be constructed.

EDM (the ASC algorithm in our implementation) algorithms are well-researched, each meant to solve a different type of problem. If we choose to implement this framework in a massive 2-D array (say 100×100), we might choose to only investigate coupling locally, leaving us with a sparse EDM. This system might demand a different method to deal with highly sparse EDMs. The freedom to choose the ASC algorithm makes the framework highly modular to any number of nonidealities in the EDM. Many EDM applications, especially those discussed in [26], include a mask matrix as a design parameter. We had success with banded mask matrices that decay exponentially, but, perhaps, another system will demand a different structure.

VIII. CONCLUSION

In this work, we presented a framework for reconstructing the shape of flexible phased arrays based on mutual coupling measurements among elements. This autonomous shape reconstruction is implemented in two steps: we present Spiral Match, a candidate for the first step, and discuss a semidefinite programming solution for the second step. Both steps can be replaced with other algorithms, enabling a level of modularity that we hope will make this framework both flexible and more accurate for particular systems. We demonstrated the accuracy of this approach on two 2.5-GHz passive phased arrays: one with a dipole and another with a patch antenna. Finally, we also demonstrated our approach in a flexible RFIC phased array. The accuracy achieved in the integrated circuit array reconstruction was $\approx 6\%$ of one wavelength. We believe

this will be sufficiently accurate for calibration-free, real-time beamforming, beamsteering, or focusing arrays. This article can serve as the beginning of a broad study into shape reconstruction algorithms and the diverse applications that they make possible. This is included but not limited to high-element arrays, strongly asymmetric shapes, stretchable arrays, 2-D arrays, and large distributed systems. We believe that mutual coupling measurements are sufficient for reconstructing array shapes in all of these circumstances and offering exciting possibilities in the future.

APPENDIX

A. Recursive Wrap Correction

The input to RWC, R, is defined as

$$R_{mn} = \text{floor}\left(\frac{E_{mn}^2}{\lambda}\right). \tag{19}$$

The problem of phase wrapping implies that R_{mn} is occasionally one or two phase wraps greater or less than the true number.

RWC takes place in two steps: recursive error correction and matrix selection.

1) Recursive Error Correction: The root method of this step, $\Theta(R)$, is a recursive algorithm, which inputs a (potentially) erroneous phase wrap matrix, R, and outputs either.

1) Itself, if R is free of errors. This is the canonical "base case."
2) $[\Theta(R^1), \Theta(R^2)]$, where R^1 and R^2 are two options for matrices that correct a single rule violation in R.

A matrix, R, has potentially many rule violations; each violation is associated with two potential corrections. Thus, recursive error correction involves generating and traversing a binary tree of matrices, where R is the highest parent node and the terminal nodes form a set, $\{R'\}$, of error-free alternatives to R.

$\Theta(R)$ begins by searching R, starting on the two inner diagonals to the right and left of the main diagonal ($\{R_{mn} \forall |m - n| = 1\}$) and ending at the two corner elements ($\{R_{mn} \forall |m - n| = N - 1\}$). Each element is checked for the following two possible rule violations:

1) discontinuity (i.e., $|R_{m,n} - R_{m,n+1}| > a$);
2) wrong direction (i.e., $R_{m,n} > R_{m,n+1}$).

The exact conditions of these violations (how discontinuity is defined, in what circumstances the direction is "wrong," and so on) will depend on the system that this algorithm is being implemented. Our system consisted of antennas separated by 0.6λ, thus defining "discontinuity" as a difference in wrap count between mutual matrix elements greater than 1 ($a = 1$). We also required that wrap counts strictly increase for increases in $|m - n|$ ("Wrong direction").

When an error is discovered, the algorithm breaks out of the search and begins a new iteration of $\Theta(R)$ with two alternatives as inputs. These two alternatives are new matrices, R^1 and R^2, each with a single element changed that simultaneously corrects the rule violation and does not introduce a new violation.

Recursion continues until all alternatives are error-free or a stop condition is reached. The rule violations and corrections are defined in a way that the stop condition is rarely reached. The result of this process is a set, $\{R'\}$, of correct phase wrap matrices that are alternatives to the original input, R. We then move on to the next phase, matrix selection, to pick our final phase wrap matrix, R'.

2) Matrix Selection: The first phase of matrix selection is to cut matrices that violate any of the following "global" criteria (ordered from most important to least):

1) duplication (i.e., $R'_k = R'_l, k \neq l$);
2) absolute distance limits;
3) symmetry (i.e., $R'_k \neq R'_k{}^T$).

Cuttings take place in these three stages. If any stage results in the cutting of all but one option, that option becomes R'. If any stage results in the cutting of *all* options, the cuts do not take place, and the algorithm moves to the next stage.

If, after these three rounds of cuts, there are still multiple options, voting takes place based on a set metric. Examples of metrics include the following.

1) *Curvature Discontinuity:* Favor matrices that reflect constant curvature conditions.
2) *Symmetry:* Favor the "most symmetric" matrix. This obviously only applies if the third round of cuts does not take place.
3) *Change:* Favor the matrix that is closest to the original.

If the system possesses constraints that can be leveraged, a metric can be designed to pick the phase wrap map that most aligns with that constraint. In our case, we opted to use symmetry if the last cut does not take place and curvature discontinuity otherwise.

As a final point, it is worth remembering that the conditions for arriving at this point are rare. In the vast majority of cases, the original input, R, is free of rule violations and, thus, is also the output R'—these metrics and conditions having absolutely no impact on the outcome. RWC was so seldom used that we failed to have a dataset large enough to accurately test for the best metric. On the other hand, in the case where an erroneous phase wrap matrix is produced by the second iteration of Spiral Match, the best that we can hope for is a realistic alternative that can correct for phase wrapping errors.

Acknowledgment

References

[1] B. Yang, Z. Yu, J. Lan, R. Zhang, J. Zhou, and W. Hong, "Digital beamforming-based massive MIMO transceiver for 5G millimeter-wave communications," *IEEE Trans. Microw. Theory Techn.*, vol. 66, no. 7, pp. 3403–3418, Jul. 2018.

[2] A. Natarajan, A. Komijani, X. Guan, A. Babakhani, and A. Hajimiri, "A 77-GHz phased-array transceiver with on-chip antennas in silicon: Transmitter and local LO-path phase shifting," *IEEE J. Solid-State Circuits*, vol. 41, no. 12, pp. 2807–2819, Dec. 2006.

[3] R. E. McIntosh, S. J. Frasier, and J. B. Mead, "FOPAIR: A focused array imaging radar for ocean remote sensing," *IEEE Trans. Geosci. Remote Sens.*, vol. 33, no. 1, pp. 115–124, Jan. 1995.

[4] B. Bräutigam, J. H. González, M. Schwerdt, and M. Bachmann, "TerraSAR-X instrument calibration results and extension for TanDEM-X," *IEEE Trans. Geosci. Remote Sens.*, vol. 48, no. 2, pp. 702–715, Feb. 2010.

[5] K. Sengupta and A. Hajimiri, "A 0.28 THz power-generation and beam-steering array in CMOS based on distributed active radiators," *IEEE J. Solid-State Circuits*, vol. 47, no. 12, pp. 3013–3031, Dec. 2012.

[6] J. Schoebel et al., "Design considerations and technology assessment of phased-array antenna systems with RF MEMS for automotive radar applications," *IEEE Trans. Microw. Theory Techn.*, vol. 53, no. 6, pp. 1968–1975, Jun. 2005.

[7] M. Gal-Katziri, A. Fikes, F. Bohn, B. Abiri, M. R. Hashemi, and A. Hajimiri, "Scalable, deployable, flexible phased array sheets," in *IEEE MTT-S Int. Microw. Symp. Dig.*, Aug. 2020, pp. 1085–1088.

[8] R. Fatemi, A. Khachaturian, and A. Hajimiri, "A nonuniform sparse 2-D large-FOV optical phased array with a low-power PWM drive," *IEEE J. Solid-State Circuits*, vol. 54, no. 5, pp. 1200–1215, May 2019.

[9] R. Fatemi, B. Abiri, A. Khachaturian, and A. Hajimiri, "High sensitivity active flat optics optical phased array receiver with a two-dimensional aperture," *Opt. Exp.*, vol. 26, no. 23, pp. 29983–29999, Nov. 2018. [Online]. Available: http://www.opticsexpress.org/abstract.cfm?URI=oe-26-23-29983, doi: 10.1364/OE.26.029983.

[10] L. Bailin, "The radiation field produced by a slot in a large circular cylinder," *IRE Trans. Antennas Propag.*, vol. 3, no. 3, pp. 128–137, Jul. 1955.

[11] J. Eberle, C. Levis, and D. McCoy, "The flared slot: A moderately directive flush-mounted broad-band antenna," *IRE Trans. Antennas Propag.*, vol. 8, no. 5, pp. 461–468, Sep. 1960.

[12] E. Jones and J. Shimizu, "A wide-band transverse-slot flush-mounted array," *IRE Trans. Antennas Propag.*, vol. 8, no. 4, pp. 401–407, Jul. 1960.

[13] H. Kobayashi, "Simple calculation method for conformal beam-scanning array pattern," in *Proc. 13th Eur. Conf. Antennas Propag. (EuCAP)*, 2019, pp. 1–5.

[14] F. Rigobello, G. Mansutti, M. S. Khan, and A.-D. Capobianco, "Pattern recovering of conformal antenna array for strongly deformed surfaces," in *Proc. 11th Eur. Conf. Antennas Propag. (EUCAP)*, Mar. 2017, pp. 869–871.

[15] L. I. Vaskelainen, "Iterative least-squares synthesis methods for conformal array antennas with optimized polarization and frequency properties," *IEEE Trans. Antennas Propag.*, vol. 45, no. 7, pp. 1179–1185, Jul. 1997.

[16] C.-M. Seong, M.-S. Kang, C.-S. Lee, and D.-C. Park, "Conformal array pattern synthesis on a curved surface with quadratic function using adaptive genetic algorithm," in *Proc. Asia–Pacific Microw. Conf. Proc. (APMC)*, Nov. 2013.

[17] R. J. Allard, D. H. Werner, and P. L. Werner, "Radiation pattern synthesis for arrays of conformal antennas mounted on arbitrarily-shaped three-dimensional platforms using genetic algorithms," *IEEE Trans. Antennas Propag.*, vol. 51, no. 5, pp. 1054–1062, May 2003. [Online]. Available: https://ieeexplore.ieee.org/stamp/stamp.jsp?tp=&arnumber=1208512

[18] R. L. Haupt, "Genetic algorithm applications for phased arrays," *Appl. Comput. Electromagn. Soc. J.*, vol. 21, no. 3, pp. 325–336, Nov. 2006.

[19] M. R. M. Hashemi et al., "A flexible phased array system with low areal mass density," *Nature Electron.*, vol. 2, no. 5, pp. 195–205, May 2019, doi: 10.1038/s41928-019-0247-9.

[20] D. E. Williams, C. Dorn, S. Pellegrino, and A. Hajimiri, "Origami-inspired shape-changing phased array," in *Proc. 50th Eur. Microw. Conf. (EuMC)*, Utrecht, The Netherlands, Jan. 2021, pp. 344–347.

[21] A. C. Fikes, A. Safaripour, F. Bohn, B. Abiri, and A. Hajimiri, "Flexible, conformal phased arrays with dynamic array shape self-calibration," in *IEEE MTT-S Int. Microw. Symp. Dig.*, Jun. 2019, pp. 1458–1461.

[22] B. D. Braaten et al., "A self-adapting flexible (SELFLEX) antenna array for changing conformal surface applications," *IEEE Trans. Antennas Propag.*, vol. 61, no. 2, pp. 655–665, Feb. 2013.

[23] C. Shipley and D. Woods, "Mutual coupling-based calibration of phased array antennas," in *Proc. IEEE Int. Conf. Phased Array Syst. Technol.*, May 2000, pp. 529–532.

[24] D. Bekers, R. van Dijk, and F. van Vliet, "Mutual-coupling based phased-array calibration: A robust and versatile approach," in *Proc. IEEE Int. Symp. Phased Array Syst. Technol.*, Oct. 2013, pp. 630–637.

[25] O. S. Mizrahi, A. Fikes, and A. Hajimiri, "Flexible phased array shape reconstruction," in *IEEE MTT-S Int. Microw. Symp. Dig.*, 2021.

[26] I. Dokmanic, R. Parhizkar, J. Ranieri, and M. Vetterli, "Euclidean distance matrices: Essential theory, algorithms, and applications," *IEEE Signal Process. Mag.*, vol. 32, no. 6, pp. 12–30, Nov. 2015, doi: 10.1109/MSP.2015.2398954.

[27] S. Haykin and M. Moher, *Modern Wireless Communication*, 1st ed. Upper Saddle River, NJ, USA: Prentice-Hall, 2004.

[28] M. Grant and S. Boyd. (Mar. 2014). *CVX: MATLAB Software for Disciplined Convex Programming, Version 2.1.* [Online]. Available: http://cvxr.com/cvx

Austin Fikes (Graduate Student Member, IEEE) received the B.S. degree in engineering from the Harvey Mudd College, Claremont, CA, USA, in 2016, and the M.S. degree in electrical engineering from the California Institute of Technology (Caltech), Pasadena, CA, USA, in 2018, where he is currently pursuing the Ph.D. degree at the Caltech Holistic Integrated Circuit Laboratory.

His research focuses on decentralized, large-scale, microwave arrays with novel form factors.

Oren S. Mizrahi (Graduate Student Member, IEEE) received the B.S. degree in electrical and computer engineering and the B.S. degree in biomedical engineering with a minor in mathematics from Duke University, Durham, NC, USA, in 2019, and the M.S. degree in electrical engineering from the California Institute of Technology (Caltech), Pasadena, CA, USA, in 2021, where he is currently pursuing the Ph.D. degree at the Caltech Holistic Integrated Circuit Laboratory.

He is interested in high-dimensional systems, imaging, sensing, and flexible phased arrays.

Ali Hajimiri (Fellow, IEEE) received the B.S. degree in electronics engineering from the Sharif University of Technology, Tehran, Iran, in 1994, and the M.S. and Ph.D. degrees in electrical engineering from Stanford University, Stanford, CA, USA, in 1996 and 1998, respectively.

He was with Phillips Semiconductors, Sunnyvale, CA, USA, where he worked on a bipolar complementary metal-oxide-semiconductor (BiCMOS) chipset for global system for mobile (GSM) and cellular units from 1993 to 1994. In 1995, he was with Sun Microsystems, Sunnyvale, working on the UltraSPARC microprocessors cache RAM design methodology. In summer 1997, he was with Lucent Technologies (Bell Labs), Murray Hill, NJ, USA, where he investigated low-phase noise-integrated oscillators. In 1998, he joined the Faculty of the California Institute of Technology, Pasadena, CA, USA, where he is currently the Bren Professor of Electrical Engineering and Medical Engineering, the Director of the Microelectronics Laboratory, and the Co-Director of the Space Solar Power Project. In 2002, he co-founded Axiom Microdevices Inc., Irvine, CA, USA, whose fully integrated CMOS PA has been shipped around 400 000 000 units, and was acquired by Skyworks Inc., Irvine, in 2009. He is also a Co-Founder of GuRu Wireless Inc., Pasadena. He is the author of *Analog: Inexact Science, Vibrant Art* (2021, Early Draft), a book on fundamental principles of analog circuit design, and *The Design of Low Noise Oscillators* (Boston, MA, USA: Springer). He has authored or coauthored more than 250 refereed journal and conference technical articles. He has been granted more than 130 U.S. patents with many more pending applications. His research interests are high-speed and high-frequency integrated circuits for applications in sensors, photonics, biomedical devices, and communication systems.

Prof. Hajimiri is also a Fellow of the National Academy of Inventors (NAI). He was selected to the TR35 Top Innovator's List. He was a recipient of the Microwave Prize. He won the Feynman Prize for Excellence in Teaching, Caltech's most prestigious teaching honor, the Caltech's Graduate Students Council Teaching and Mentoring Award, and the Associated Students of Caltech Undergraduate Excellence in Teaching Award. He was the Gold medal winner of the National Physics Competition and the Bronze Medal winner of the 21st International Physics Olympiad, Groningen, The Netherlands. He was a co-recipient of the IEEE Journal of Solid-State Circuits Best Paper Award, the International Solid-State Circuits Conference (ISSCC) Jack Kilby Outstanding Paper Award, the RFIC Best Paper Award, the IMS Best Advance Practices Awards, a two-time co-recipient of the CICC Best Paper Award, and a three-time winner of the IBM Faculty Partnership Award, the National Science Foundation CAREER Award, and the Okawa Foundation Award. He was recognized as one of the top-ten contributors to ISSCC. He has served as a Distinguished Lecturer of the IEEE Solid-State and Microwave Societies. He has served on the Technical Program Committee of the International Solid-State Circuits Conference (ISSCC), as an Associate Editor of the IEEE JOURNAL OF SOLID-STATE CIRCUITS (JSSC) and IEEE TRANSACTIONS ON CIRCUITS AND SYSTEMS (TCAS) II, a member of the Technical Program Committees of the International Conference on Computer Aided Design (ICCAD), a Guest Editor of the IEEE TRANSACTIONS ON MICROWAVE THEORY AND TECHNIQUES, and a Guest Editorial Board Member of *Transactions of Institute of Electronics, Information and Communication Engineers of Japan* (IEICE).